Interferenceless Polarization Splitting Through Nanoscale van der Waals Heterostructures

Shahnawaz Shah,[1,2] Xiao Lin,[3,*] Lian Shen,[1,2] Maturi Renuka,[1,2] Baile Zhang,[3,4] and Hongsheng Chen[1,2]

[1]*Key Laboratory of Advanced Micro/Nano Electronic Devices & Smart Systems of Zhejiang, Zhejiang University, Hangzhou 310027, China*

[2]*The Electromagnetics Academy at Zhejiang University, College of Information Science and Electronic Engineering, Zhejiang University, Hangzhou 310027, China*

[3]*Division of Physics and Applied Physics, School of Physical & Mathematical Sciences, Nanyang Technological University, Singapore 637371, Singapore*

[4]*Centre for Disruptive Photonic Technologies, NTU, Singapore 637371, Singapore*

(Received 13 March 2018; revised manuscript received 29 May 2018; published 14 September 2018)

The ability to control the polarization of light at the extreme nanoscale has long been a major scientific and technological goal for photonics. Here we predict the phenomenon of polarization splitting through van der Waals heterostructures of nanoscale thickness, such as graphene-hexagonal boron nitride heterostructures, at infrared frequencies (near 25.35 THz). The underlying mechanism is that the designed heterostructures possess an effective relative permittivity with its in-plane (out-of-plane) component being unity (zero); such heterostructures are transparent to transverse-electric (TE) waves while opaque to transverse-magnetic (TM) waves, without resorting to the interference effect. Moreover, the predicted phenomenon is insensitive to incident angles. Our work thus indicates that van der Waals heterostructures are a promising nanoscale platform for the manipulation of light, such as the design of polarization beam nanosplitters and ϵ-near-zero materials, and the exploration of superscattering for TM waves and zero scattering for TE waves from deep-subwavelength nanostructures.

DOI: 10.1103/PhysRevApplied.10.034025

I. INTRODUCTION

The emergence of layered two-dimensional materials [1–3] and van der Waals heterostructures [4,5], such as graphene [6–13], hexagonal boron nitride (*h*-BN) [14–21] and graphene–*h*-BN heterostructures [22–27], has ignited numerous nanophotonic studies of both fundamental and applied nature. Due to their appealing optical properties, researchers have tried to control the flow of light at the nanoscale and even at the atomic scale [1,2,6,7,28]. For example, it was recently reported possible to design the surface cloaks [29] and perfect absorbers [30] using a graphene monolayer, and to realize the negative refraction in graphene–*h*-BN heterostructures with a thickness of several nanometers [26]. One remaining open challenge is to control the polarization of light at the extreme nanoscale, especially to achieve the total transmittance for one linearly polarized wave (such as a TE or *s*-polarized wave) and the total reflectance for the other linearly polarized wave (a TM or *p*-polarized wave) within a wide range of incident angles. Below, this exotic phenomenon is referred to as the perfect polarization splitting, which is highly sought after but has not been realized through nanostructures without external magnetic fields [28]. The perfect polarization splitting is of paramount importance to photonics. This is because polarization is an inherent characteristic of light and its flexible control can result in many intriguing phenomena and unique applications [31,32]. One typical application of polarization splitting is polarization beam splitters, which have been widely used in photonic systems, including optical communications, imaging processing, and integrated photonic circuits [32–35]. Conventional polarization beam splitters are designed based on the birefringence of anisotropic materials [35], Brewster effect [35,36], light interference in optically thin films [35], photonic crystals [37,38], metamaterials [39,40], metasurfaces [41], and so on. Although these polarization beam splitters can have good performance in the separate control of differently polarized light, they still require a thickness of the order of the wavelength scale (e.g., around one-tenth of the wavelength based on metasurfaces [41]).

In this work, we predict the polarization splitting of linearly polarized waves through van der Waals heterostructures, such as graphene–*h*-BN heterostructures, with a nanoscale thickness (<10 nm for the example given

*xiaolinbnwj@ntu.edu.sg

below) at the infrared regime (near 25.35 THz). In other words, for the ideal lossless case, the total reflectance of TM waves and the total transmittance of TE waves can be simultaneously achieved, for arbitrary incident angle. This is because the graphene–*h*-BN heterostructures can be designed to have an effective permittivity with its in-plane (out-of-plane) component being unity (zero). This way, the designed heterostructures is transparent to TE waves while opaque to TM waves, without the help of the interference effect. We note that the interferenceless effect was once used to achieve the perfect absorption by a van der Waals crystal [42,43]; our work shall be a further development of the interferenceless effect [42,43] in the control of the polarization of light. With the consideration of realistic material loss, the polarization splitting, i.e., with a high ratio (>100) of reflectance or transmittance between different polarized light, can still be maintained within a wide range of incident angles near 25.35 THz.

II. PERFECT POLARIZATION SPLITTING OF TM AND TE WAVES

We start with the schematic illustration of the phenomenon of perfect polarization splitting for TM and TE waves in Fig. 1. The wave is incident from region 1 with a relative permittivity of $\varepsilon_{1,r} = 1$ (i.e., air) and transmits into region 2 with $\bar{\bar{\varepsilon}}_{2,r} = (\varepsilon_{||,r}, \varepsilon_{||,r}, \varepsilon_{\perp,r})$. From the classic electromagnetic theory [44], the reflection coefficients for TM and TE waves are derived as

$$r_{1|2}^{\mathrm{TM}} = \frac{\cos\theta\varepsilon_{\parallel,r} - \sqrt{\varepsilon_{||,r} - (\varepsilon_{||,r}/\varepsilon_{\perp,r})\sin^2\theta}}{\cos\theta\varepsilon_{\parallel,r} + \sqrt{\varepsilon_{||,r} - (\varepsilon_{||,r}/\varepsilon_{\perp,r})\sin^2\theta}} \tag{1}$$

$$r_{1|2}^{\mathrm{TE}} = \frac{\cos\theta - \sqrt{\varepsilon_{||,r} - \sin^2\theta}}{\cos\theta + \sqrt{\varepsilon_{||,r} - \sin^2\theta}}, \tag{2}$$

where θ is the incident angle. Correspondingly, the transmission coefficients for TM and TE waves are $t_{1|2}^{\mathrm{TM}} = 2\varepsilon_{\parallel,r}\cos\theta/\{\cos\theta\varepsilon_{\parallel,r} + [\varepsilon_{||,r} - (\varepsilon_{||,r}/\varepsilon_{\perp,r})\sin^2\theta]^{1/2}\}$ and $t_{1|2}^{\mathrm{TE}} = 2\cos\theta/[\cos\theta + (\varepsilon_{||,r} - \sin^2\theta)^{1/2}]$, respectively; the ideal lossless case, the transmittance of TE waves is equal to $T^{\mathrm{TE}} = 1 - |r_{1|2}^{\mathrm{TE}}|^2$. When region 2 is an isotropic medium (i.e., $\varepsilon_{||,r} = \varepsilon_{\perp,r}$), Eqs. (1) and (2) indicate that there will be nonzero reflectance for both TM and TE waves [see Fig. 1(a)], except when the incident angle is the Brewster angle for TM waves [36,44].

When region 2 is a uniaxial medium (i.e., $\varepsilon_{||,r} \neq \varepsilon_{\perp,r}$), we find that it is possible to achieve the perfect polarization splitting with $|r_{1|2}^{\mathrm{TM}}| = 1$ and $r_{1|2}^{\mathrm{TE}} = 0$, i.e., total reflectance (transmittance) for TM (TE) waves, for arbitrary incident angle; see Fig. 1(b). From Eqs. (1) and (2), the corresponding condition is $\varepsilon_{||,r} = 1$ and $\varepsilon_{\perp,r} = 0$. To our knowledge,

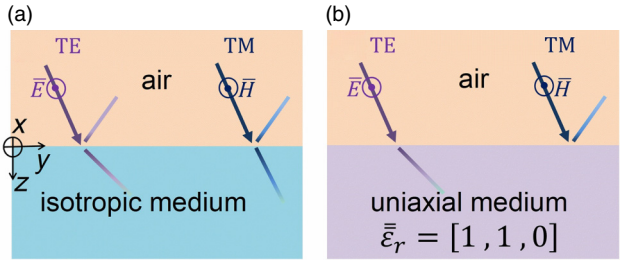

FIG. 1. Interferenceless perfect polarization splitting of TM and TE waves at a single interface. The reflectance and transmittance of TM and TE waves at the interface (a) of air and semi-infinite isotropic medium and (b) of air and semi-infinite uniaxial medium are schematically shown for comparison. The perfect polarization splitting, independent of the incidence angle, can be achieved via a uniaxial medium with a relative permittivity of $\bar{\bar{\varepsilon}}_r = [\varepsilon_{||,r}, \varepsilon_{||,r}, \varepsilon_{\perp,r}]$, where $\varepsilon_{||,r} = 1$ and $\varepsilon_{\perp,r} = 0$.

this condition has not been directly discussed for the realization of perfect polarization splitting. We note that Ref. [39] also used uniaxial metamaterials to obtain the perfect polarization splitting. However, while the optical axis of our uniaxial medium is perpendicular to the interface (i.e., along the z direction), the optical axis of their uniaxial medium [39] is parallel to the interface (i.e. along the y direction). Consequently, their perfect polarization splitting can be achieved only at certain values of ϕ (i.e., $\phi = 0$ in Ref. [39]), where ϕ is the angle between the incident plane (which contains the surface normal, i.e., the z axis, and the propagation wave vector) and the plane containing the surface normal and the optical axis of uniaxial medium (i.e., the y-z plane). In contrast, our proposed structure has no such limit, i.e., the perfect polarization splitting is independent of ϕ, due to the rotational symmetry of our structure with respect to the surface normal. In addition, our work is different from Refs. [42,43], which discussed the condition to achieve $|r_{1|2}^{\mathrm{TE}}| = 0$ or $|r_{1|2}^{\mathrm{TM}}| = 1$, i.e., total reflectance for TM waves or total transmittance for TE waves at *different* frequencies, instead of the same frequency.

Moreover, for the perfect polarization splitting can also be achieved through a thin slab of such uniaxial medium [i.e., $\bar{\bar{\varepsilon}}_{2,r} = (1,1,0)$]. For conceptual illustration, we assume the uniaxial slab with a thickness of d is surrounded by air, i.e., $\varepsilon_{3,r} = \varepsilon_{1,r} = 1$. This way, the reflection and transmission coefficients of TE and TM waves through a uniaxial slab are derived as [44]

$$r_{1|3}^{\mathrm{TM}} = r_{1|2}^{\mathrm{TM}} + \frac{t_{1|2}^{\mathrm{TM}} r_{2|3}^{\mathrm{TM}} t_{2|1}^{\mathrm{TM}} e^{2ik_{z,2}^{\mathrm{TM}} d}}{1 - r_{2|1}^{\mathrm{TM}} r_{2|3}^{\mathrm{TM}} e^{2ik_{z,2}^{\mathrm{TM}} d}}, \tag{3}$$

$$t_{1|3}^{\mathrm{TM}} = \frac{t_{1|2}^{\mathrm{TM}} t_{2|3}^{\mathrm{TM}} e^{ik_{z,2}^{\mathrm{TM}} d}}{1 - r_{2|1}^{\mathrm{TM}} r_{2|3}^{\mathrm{TM}} e^{2ik_{z,2}^{\mathrm{TM}} d}}, \tag{4}$$

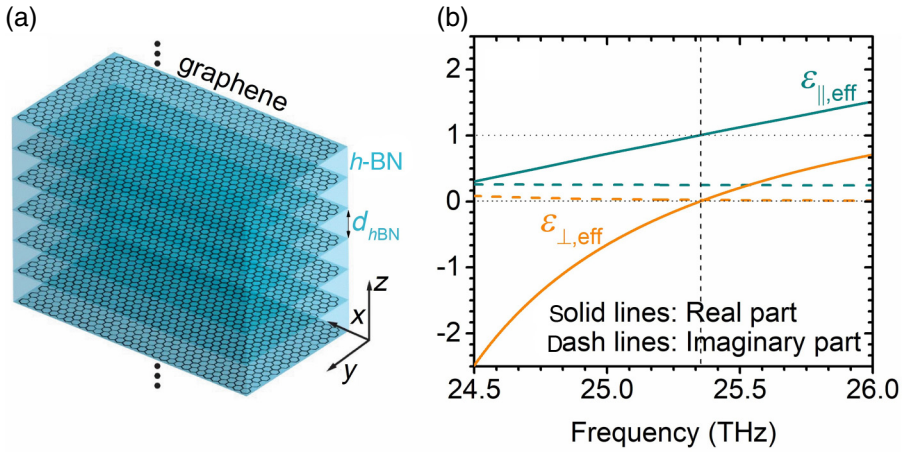

FIG. 2. Construction of the uniaxial medium with an effective relative permittivity of (1,1,0) via graphene–*h*-BN heterostructures. (a) Schematic illustration of graphene–*h*-BN heterostructures. (b) Effective relative permittivity of graphene–*h*-BN heterostructures, i.e., $\bar{\bar{\varepsilon}}_{\mathrm{eff},r} = [\varepsilon_{||,\mathrm{eff}}, \varepsilon_{||,\mathrm{eff}}, \varepsilon_{\perp,\mathrm{eff}}]$. The effective relative permittivity of (1,1,0) is achieved at 25.35 THz. Here $d_{h\mathrm{BN}} =$ 9 nm; the monolayer graphene, with a thickness of 0.35 nm, has a chemical potential of $\mu_c = 0.1484$ eV and an electron mobility of 30 000 $\mathrm{cm^2\,V^{-1}\,s^{-1}}$.

$$r_{1|3}^{\mathrm{TE}} = r_{1|2}^{\mathrm{TE}} + \frac{t_{1|2}^{TE} r_{2|3}^{\mathrm{TE}} t_{2|1}^{\mathrm{TE}} \mathrm{e}^{2ik_{z,2}^{\mathrm{TE}} d}}{1 - r_{2|1}^{\mathrm{TE}} r_{2|3}^{\mathrm{TE}} \mathrm{e}^{2ik_{z,2}^{\mathrm{TE}} d}}, \tag{5}$$

$$t_{1|3}^{\mathrm{TE}} = \frac{t_{1|2}^{\mathrm{TE}} t_{2|3}^{\mathrm{TE}} \mathrm{e}^{ik_{z,2}^{\mathrm{TE}} d}}{1 - r_{2|1}^{\mathrm{TE}} r_{2|3}^{\mathrm{TE}} \mathrm{e}^{2ik_{z,2}^{\mathrm{TE}} d}}. \tag{6}$$

In the above equations, $t_{2|1}^{\mathrm{TM}} = t_{2|3}^{\mathrm{TM}} = 2[\varepsilon_{||,r} - (\varepsilon_{||,r}/\varepsilon_{\perp,r})\sin^2\theta]^{1/2}/\{\cos\theta\varepsilon_{||,r} + [\varepsilon_{||,r} - (\varepsilon_{||,r}/\varepsilon_{\perp,r})\sin^2\theta]^{1/2}\}$, $r_{2|1}^{\mathrm{TM}} = r_{2|3}^{\mathrm{TM}} = -r_{1|2}^{\mathrm{TM}}$, $t_{2|1}^{\mathrm{TE}} = t_{2|3}^{\mathrm{TE}} = 2(\varepsilon_{||,r} - \sin^2\theta)^{1/2}/[\cos\theta + (\varepsilon_{||,r} - \sin^2\theta)^{1/2}]$, $r_{2|1}^{\mathrm{TE}} = r_{2|3}^{\mathrm{TE}} = -r_{1|2}^{\mathrm{TE}}$, $k_{z,2}^{\mathrm{TM}} = (\omega)/c[\varepsilon_{||,r} - (\varepsilon_{||,r}/\varepsilon_{\perp,r})\sin^2\theta]^{1/2}$, $k_{z,2}^{\mathrm{TE}} = (\omega/c)(\varepsilon_{||,r} - \sin^2\theta)^{1/2}$, ω is the angular frequency, and c is the light speed in free space.

One has that when a plane wave goes through a uniaxial slab with $\bar{\bar{\varepsilon}}_{2,r} = (1,1,0)$, for an arbitrary incident angle, the reflectance of TM waves is unity (i.e., $R^{\mathrm{TM}} = |r_{1|3}^{\mathrm{TM}}|^2 = 1$) and the reflectance of TE waves is zero (i.e., $R^{\mathrm{TE}} = |r_{1|3}^{\mathrm{TE}}|^2 = 0$). Both R^{TM} and T^{TE} are independent of the slab thickness. Such behavior can be explained by the interferenceless effect. For $r_{1|3}^{\mathrm{TM}}$ in Eq. (3), since $t_{1|2}^{\mathrm{TM}} = 0$ for arbitrary incident angle, one has $R^{\mathrm{TM}} = |r_{1|3}^{\mathrm{TM}}|^2 = |r_{1|2}^{\mathrm{TM}}|^2 = 1$, which is independent of the slab thickness d. Similarly, for $r_{1|3}^{\mathrm{TE}}$ in Eq. (5), since $r_{1|2}^{\mathrm{TE}} = -r_{2|3}^{\mathrm{TE}} = 0$ for arbitrary incident angle, one has $R^{\mathrm{TE}} = |r_{1|3}^{\mathrm{TE}}| = 0$ (and thus $T^{\mathrm{TE}} = 1 - R^{\mathrm{TE}} = 1$), which is also independent of the slab thickness d. This underlying new mechanism without resorting to the interference effect, different from previous works [33–39], may provide the possibility to design the ultrathin polarization splitter of nanoscale thickness; see the discussions below.

III. RESULTS AND DISCUSSION

Figure 2 shows that graphene–*h*-BN heterostructures are a viable platform to construct the uniaxial medium with $\bar{\bar{\varepsilon}}_{2,r} = (1,1,0)$ near *h*-BN's first reststrahlen band (i.e., at 25.35 THz). Figure 2(a) schematically shows the heterostructure, where the unit cell contains a monolayer graphene and a *h*-BN slab with a thickness of $d_{h\mathrm{BN}} =$ 9 nm. The experimental data of an isotopically enriched *h*-BN slab are adopted to model *h*-BN's relative permittivity [45,46], i.e., $\bar{\bar{\varepsilon}}_{r,h\mathrm{BN}} = (\varepsilon_{||,h\mathrm{BN}}, \varepsilon_{||,h\mathrm{BN}}, \varepsilon_{\perp,h\mathrm{BN}})$; see Appendix A. Since the studied wave has the component of wave vector parallel to the interface less than ω/c, the nonlocal effect of graphene is minor and can be neglected [47]; the Kubo formula is thus adopted to model the surface conductivity σ_s of graphene [47]; see Appendix A. Graphene has a chemical potential of $\mu_c = 0.1484$ eV and a conservative electron mobility of 30 000 $\mathrm{cm^2\,V^{-1}\,s^{-1}}$ [48,49],

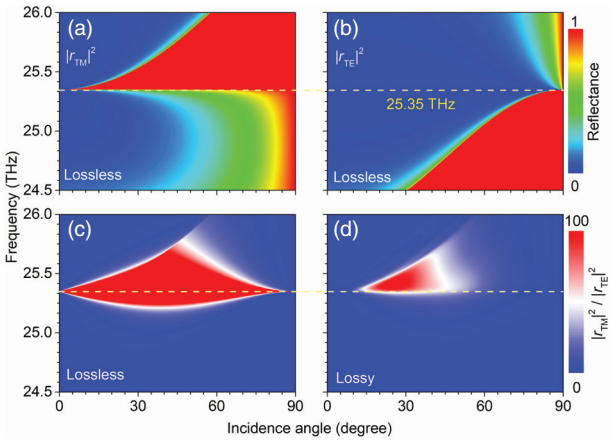

FIG. 3. Polarization splitting of TM and TE waves at the interface of the air and semi-infinite graphene–*h*-BN heterostructure. The setup of the heterostructure is the same as Fig. 2(b). Reflectance for (a) TM and (b) TE waves. (c) Ratio of reflectance between TM and TE waves. The perfect polarization splitting occurs at 25.35 THz. The material loss in (a)–(c) is neglected for conceptual illustration, i.e., the imaginary part of permittivity is artificially set to be zero. (d) The high ratio (>100) of reflectance between TM and TE waves is achieved in a relatively wide range of incidence angles (i.e., [20°, 30°]) near 25.35 THz, when the realistic material loss is considered. For the realistic lossy case, all transmitted waves are absorbed in the semi-infinite graphene–*h*-BN heterostructure; this way, only the reflectance ratio is suitable to characterize the polarization splitting.

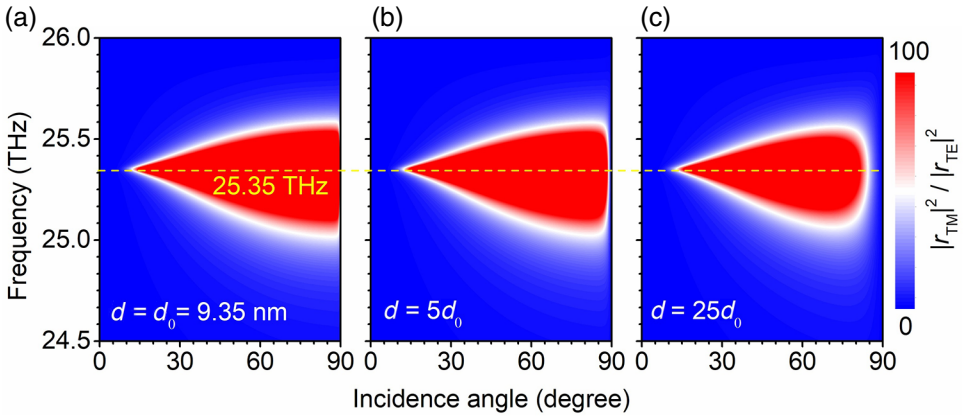

FIG. 4. Polarization splitting of TM and TE waves via a thin slab of graphene–*h*-BN heterostructure. The graphene–*h*-BN heterostructure, with its setup the same as Fig. 3(b), has a thickness of d; the material loss is considered. Ratio of reflectance between TM and TE waves when d is equal to (a) d_0, (b) $5d_0$, (c) $25d_0$, where $d_0 = 9.35$ nm. For the reflected waves, the performance of polarization splitting near 25.35 THz becomes better with the use of a thinner slab.

which characterizes the loss in graphene, is assumed. This way, the effective relative permittivity of graphene can be described by $\bar{\bar{\varepsilon}}_{r,\mathrm{gra}} = (\varepsilon_{||,\mathrm{gra}}, \varepsilon_{||,\mathrm{gra}}, \varepsilon_{\perp,\mathrm{gra}})$, where $\varepsilon_{||,\mathrm{gra}} = 1 + (i\sigma_s/\omega\varepsilon_0 d_{\mathrm{gra}})$ [6] and $\varepsilon_{\perp,\mathrm{gra}} = 3$ [50], the graphene thickness is $d_{\mathrm{gra}} = 0.35$ nm [51], and ε_0 is the permittivity of free space.

Since the thickness of the unit cell of the graphene–*h*-BN heterostructure, i.e., $d_0 = d_{\mathrm{gra}} + d_{h\mathrm{BN}} = 9.35$ nm, is much smaller than the wavelength of light considered ($\lambda > 10$ μm), Fig. 6 in the Appendix B shows that the effective medium theory [44] is applicable to model the designed heterostructures. The effective relative permittivity $\bar{\bar{\varepsilon}}_{r,\mathrm{eff}} = [\varepsilon_{||,\mathrm{eff}}, \varepsilon_{||,\mathrm{eff}}, \varepsilon_{\perp,\mathrm{eff}}]$ of the designed heterostructures can be expressed as

$$\varepsilon_{\perp,\mathrm{eff}} = \frac{\varepsilon_{\perp,\mathrm{gra}}\varepsilon_{\perp,h\mathrm{BN}}(d_{\mathrm{gra}} + d_{h\mathrm{BN}})}{d_{\mathrm{gra}}\varepsilon_{\perp,h\mathrm{BN}} + d_{h\mathrm{BN}}\varepsilon_{\perp,\mathrm{gra}}}, \tag{7}$$

$$\varepsilon_{\parallel,\mathrm{eff}} = \frac{\varepsilon_{\parallel,\mathrm{gra}}.d_{\mathrm{gra}} + \varepsilon_{\parallel,h\mathrm{BN}}.d_{h\mathrm{BN}}}{d_{\mathrm{gra}} + d_{h\mathrm{BN}}}. \tag{8}$$

Since $\mathrm{Re}(\varepsilon_{\perp,h\mathrm{BN}}) = 0$ at 25.35 THz, Eq. (7) directly indicates $\mathrm{Re}(\varepsilon_{\perp,\mathrm{eff}}) \approx 0$ at 25.35 THz; this also indicates that the value of $\varepsilon_{\perp,\mathrm{gra}}$ has minor influence on the performance of our designed polarization splitting. Since $\varepsilon_{||,\mathrm{gra}} < 0$ and $\varepsilon_{||,h\mathrm{BN}} > 0$ at 25.35 THz, it is feasible to achieve $\mathrm{Re}(\varepsilon_{||,\mathrm{eff}}) = 1$ at 25.35 THz via tailoring the chemical potential of graphene from Eq. (8). By following the above design procedure, Fig. 2(b) shows that $\mathrm{Re}(\varepsilon_{\perp,\mathrm{eff}}) = 0$ and $\mathrm{Re}(\varepsilon_{||,\mathrm{eff}}) = 1$ are simultaneously achieved at 25.35 TH; due to the existence of material loss, one also has $\mathrm{Im}(\varepsilon_{\perp,\mathrm{eff}}) = 0.0225$ and $\mathrm{Im}(\varepsilon_{||,\mathrm{eff}}) = 0.2462$ at 25.35 THz.

Figure 3 shows the performance of polarization splitting of TM and TE waves at the interface of air and semi-infinite graphene–*h*-BN heterostructures. For the simplicity of conceptual demonstration, we first neglect the material loss, i.e., by artificially neglecting the imaginary part of permittivity. Figures 3(a) and 3(b) show the reflectance of TM and TE waves, respectively; Fig. 3(c) shows the ratio of reflectance between TM and TE waves. As expected, the perfect polarization splitting is achieved at 25.35 THz, independent of the incident angle. Moreover, when considering the realistic material loss, the polarization splitting with good performance ($|r_{1|3}^{\mathrm{TM}}|^2/|r_{1|3}^{\mathrm{TE}}|^2 > 100$) is still maintained in a relative wide range of incident angles (i.e., [20°, 30°]) near 25.35 THz; see Fig. 3(d). For the realistic lossy case, since all transmitted waves will be dissipated inside the semi-infinite heterostructures, only the reflectance ratio is suitable to describe the polarization

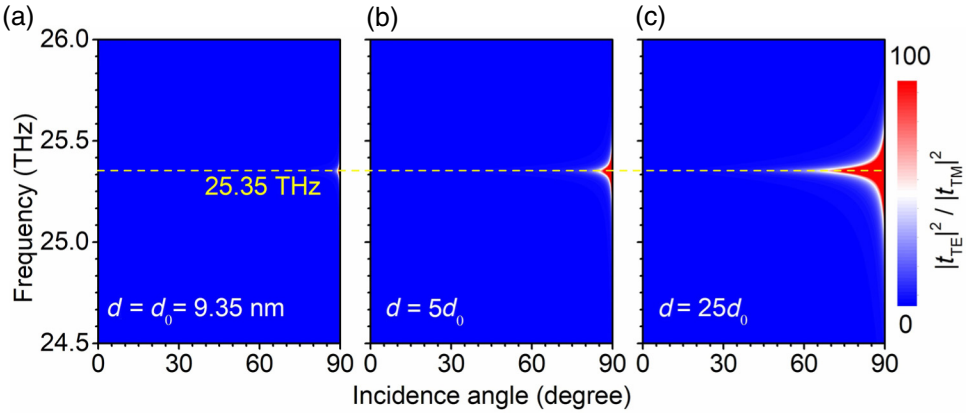

FIG. 5. Polarization splitting of TM and TE waves via a thin slab of graphene–*h*-BN heterostructure. The setup of graphene–*h*-BN heterostructures is the same as Fig. 4. Ratio of transmittance between TE and TM waves when d is equal to (a) d_0, (b) $5d_0$, (c) $25d_0$. For the transmitted waves, the performance of polarization splitting near 25.35 THz becomes better with the use of a thicker slab.

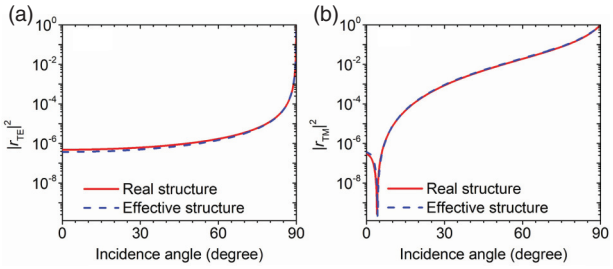

FIG. 6. Comparison of reflectance calculated from the real structure and from the effective structure at 25.35 THz. The effective structure is obtained by applying the effective medium theory to the real structure. The reflectance curves from the real and effective structures match well, both for (a) TE waves and (b) TM waves. Therefore, the effective medium theory is valid in this work. For the real structure of the graphene–*h*-BN heterostructure, the graphene is modeled by a surface conductivity of σ_s, *h*-BN is modeled by a relative permittivity of $\bar{\bar{\varepsilon}}_{r,hBN} = (\varepsilon_{||,hBN}, \varepsilon_{||,hBN}, \varepsilon_{\perp,hBN})$. For the effective structure, the whole graphene–*h*-BN heterostructure is modeled by a relative permittivity of $\bar{\bar{\varepsilon}}_{r,\text{eff}} = (\varepsilon_{||,\text{eff}}, \varepsilon_{||,\text{eff}}, \varepsilon_{\perp,\text{eff}})$; see Eqs. (7) and (8). Here $d_{hBN} = 9$ nm; the monolayer graphene has a chemical potential of $\mu_c = 0.1484$ eV and an electron mobility of 30 000 $\text{cm}^2\,\text{V}^{-1}\,\text{s}^{-1}$.

splitting in Fig. 3. This also indicates our designed structures are suitable for the perfect absorption of TM waves [42,43].

Figures 4 and 5 show the polarization splitting of TM and TE waves from an ultrathin slab of graphene–*h*-BN heterostructures. In Figs. 4 and 5, the realistic material loss is considered. For the reflected waves in Fig. 4, the performance of polarization splitting can be improved by using a thinner slab of graphene–*h*-BN heterostructure. Most importantly, the polarization splitting with $|r^{TM}_{1|3}|^2/|r^{TE}_{1|3}|^2 > 100$ can be achieved in a wide range of incident angles (i.e., [12° 90°]) near 25.35 THz, by only using an ultrathin slab with thickness $d < 10$ nm (less than 1/1000 of the wavelength in free space, i.e., $d < \lambda/1000$); see Fig. 5(a). It is actually quite unexpected to see that the performance of polarization splitting from an ultrathin slab in Fig. 4(a) is much better than from a single interface in Fig. 3(d). For the transmitted waves in Fig. 5, the performance of polarization splitting is highly dependent on the slab thickness and, in contrast to Fig. 4, can be improved by using a thicker slab. In order to gain a better performance, the thickness of the designed slab is required to be at least several hundred nanometers, such as $d \approx 250$ nm (still $d < \lambda/40$) in Fig. 5(c). For the practical design of polarizers, in addition to the performance of polarization splitting, the actual values of reflectance and transmittance are also important. For the design of polarizers with the reflected waves, there is a tradeoff for the choice of the slab thickness, since the increase of slab thickness can increase the TM reflectance [see Fig. 7(b) in Appendix C] but will degrade the performance of polarization splitting in Fig. 4. For the design of polarizers with the transmitted waves, a thick slab is always preferred, to simultaneously maintain a high TE transmittance [see Fig. 7(c) in Appendix C] and a good performance of polarization splitting in Fig. 5.

The above dependence of the performance of polarization splitting on the thickness of a slab of graphene–*h*-BN heterostructures in Figs. 4 and 5 is mainly due to the existence of material loss. When material loss exists, the value of $|r^{TM}_{1|2}| = |r^{TM}_{2|3}|$ will become nonunity, leading to

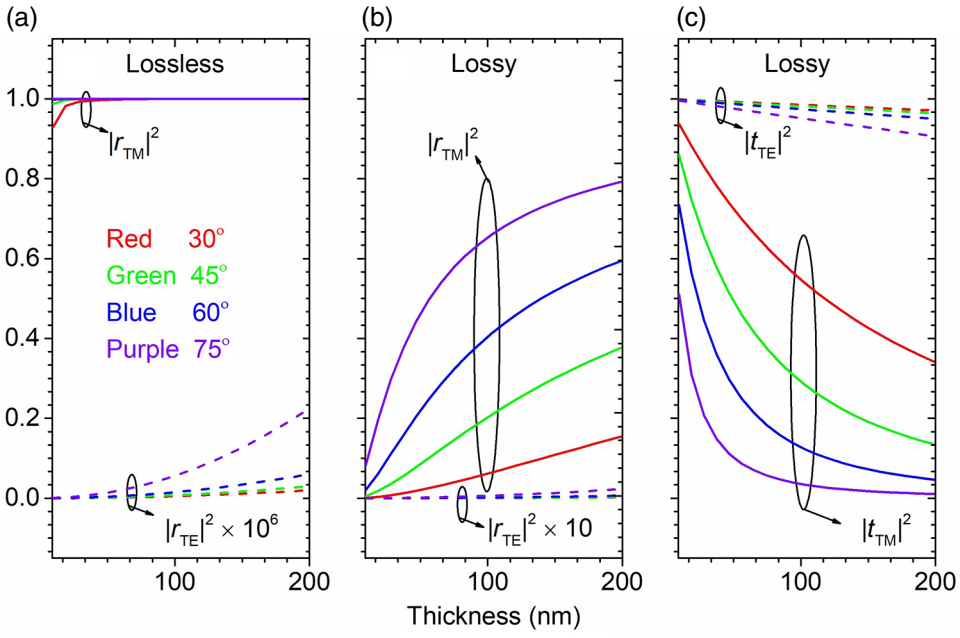

FIG. 7. Reflectance and transmittance of TE and TM waves as a function of the slab thickness at 25.35 THz. The slab is composed by the graphene–*h*-BN heterostructure and has a relative permittivity of $\bar{\bar{\varepsilon}}_{r,\text{eff}} = [\varepsilon_{||,\text{eff}}, \varepsilon_{||,\text{eff}}, \varepsilon_{\perp,\text{eff}}]$; see Eqs. (7) and (8). (a) Reflectance in the lossless case, where the imaginary part of $\bar{\bar{\varepsilon}}_{r,\text{eff}}$ is artificially neglected. For the lossless case, the sum of reflectance and transmittance is equal to 1. (b) Reflectance and (c) transmittance for the lossy case, where the realistic material loss is considered. In each panel, lines with different colors represent different incident angles; the solid lines represent the TM waves, while the dashed lines represent the TE waves.

$|r_{1|3}^{\mathrm{TM}}| \neq 1$ in Eq. (3) and $|t_{1|3}^{\mathrm{TM}}| \neq 0$ in Eq. (4); similarly, the value of $|r_{1|2}^{\mathrm{TE}}| = |r_{2|3}^{\mathrm{TE}}|$ will becomes nonzero, leading to $|r_{1|3}^{\mathrm{TE}}| \neq 0$ in Eq. (5) and $|t_{1|3}^{\mathrm{TE}}| \neq 1$ in Eq. (6). In other words, due to the material loss, there will be part of the incident field firstly transmitting into, then reflecting back and forth inside the loss uniaxial slab. This part of the field will unavoidably degrade the performance of polarization splitting, especially for the transmitted waves.

Finally, it is worth mentioning that the commercial polarizers [35] can generally operate at a relatively broad range of frequency, but only within a narrow range of incident angles. In contrast, the proposed proof-of-concept polarizers based on van der Waals heterostructures can operate within a wide range of incident angles, but only at a narrow range of frequency (near 25.35 THz). Therefore, the ideal thin polarizers, which can operate simultaneously at a broad range of frequency and within a broad range of incident angles, are worthy of further study in the future.

IV. CONCLUSION

In conclusion, we predict the interferenceless polarization splitting of linearly polarized waves with the use of van der Waals heterostructures. The underlying mechanism is that the heterostructures can be tailored to possess a relative permittivity with its in-plane (out-of-plane) component being unity (zero); then the heterostructures are intrinsically transparent (opaque) to TE (TM) waves. Most importantly, since the interferenceless mechanism does not rely on the interference effect, it provides a feasible way to achieve the polarization splitting via an ultrathin slab with its thickness down to even the nanoscale. Therefore, our work indicates that the van der Waals heterostructures are a promising and versatile platform to manipulate light in the extreme nanoscale, such as the design of polarization nanosplitters and the widely studied epsilon-near-zero materials [52,53], and to demonstrate many other exotic optical phenomena. For example, it is very desirable to simultaneously realize zero scattering for TE waves and superscattering for TM waves [21] at the same frequency; this way, the detection will be highly sensitive to the polarization of light. This might be realized by a cylindrical subwavelength structure based on a graphene–*h*-BN heterostructure, which works near the frequency where the in-plane (out-of-plane) component of the effective relative permittivity of heterostructures is unity (negative [21]).

ACKNOWLEDGMENTS

This work is sponsored by the National Natural Science Foundation of China under Grants No. 61625502, 61574127, 61601408, 61775193, and 11704332, the ZJNSF under Grant No. LY17F010008, the Top-Notch Young Talents Program of China, the Fundamental Research Funds for the Central Universities, and the Innovation Joint Research Center for Cyber-Physical-Society System, the Nanyang Technological University for Nanyang Assistant Professorship Start-Up Grant, the Singapore Ministry of Education under Grants No. MOE2015-T2-1-070 and MOE2016-T3-1-006, and Tier 1 RG174/16(S).

APPENDIX A: SURFACE CONDUCTIVITY OF GRAPHENE AND PERMITTIVITY OF *h*-BN

In this work, the Kubo formula [45] is adopted to model the surface conductivity of a graphene monolayer, i.e., $\sigma_{\mathrm{gra}} = \sigma_{\mathrm{inter}} + \sigma_{\mathrm{intra}}$, where $\sigma_{\mathrm{inter}} = ie^2 k_B T/\{\pi\hbar^2[\omega + (i/\tau)]\}\left[(\mu_c/k_B T) + 2\ln(e^{-(\mu_c/k_B T)} + 1)\right]$ and $\sigma_{\mathrm{intra}} = [ie^2(\omega + i/\tau)/\pi\hbar^2]\int_0^\infty [f_d(-x) - f_d(x)]/[(\omega + i/\tau)^2 - 4(x/\hbar)^2]dx$. In the above equations, $f_d(x) = (\mathrm{e}^{[(x-\mu_c)/k_B T]} + 1)^{-1}$ is the Fermi-Dirac distribution, $T = 300$ K, e is the electron charge, k_B is the Boltzman constant, and $\hbar$ is the reduced Plank constant. The relaxation time is $\tau = \mu_c \mu/(e v_F^2)$, where the Fermi velocity is $v_F = 1 \times 10^6$ m s^{-1}. In this work, the chemical potential is set to be $\mu_c = 0.1484$ eV and a conservative electron mobility of 30 000 cm^2 V^{-1} s^{-1} [46,47] is assumed; this way, the corresponding relaxation time is $\tau = 0.4452$ ps. The in-plane component of the relative permittivity of the graphene monolayer is obtained via $\varepsilon_{||,\mathrm{gra}} = 1 + (i\sigma_s/\omega\varepsilon_0 d_{\mathrm{gra}})$ [6], where the thickness of monolayer graphene is $d_{\mathrm{gra}} = 0.35$ nm [49]. The value of $\mathrm{Re}(\varepsilon_{||,\mathrm{gra}})$ is negative at 25.35 THz.

The uniaxial material *h*-BN is characterized by a relative permittivity of $\bar{\bar{\varepsilon}}_{r,h\mathrm{BN}} = [\varepsilon_{||,h\mathrm{BN}}, \varepsilon_{||,h\mathrm{BN}}, \varepsilon_{\perp,h\mathrm{BN}}]$, where $\varepsilon_x = \varepsilon_y = \varepsilon_{||,h\mathrm{BN}}$ and $\varepsilon_z = \varepsilon_{\perp,h\mathrm{BN}}$. The experimental data of an isotopically enriched *h*-BN slab [43,44] are adopted to model *h*-BN's relative permittivity, i.e.,

$$\varepsilon_{l,h\mathrm{BN}}(\omega) = \varepsilon_{l,\infty}\left(\frac{\omega_{l,\mathrm{LO}}{}^2 - \omega^2 - i\Gamma_l\omega}{\omega_{l,\mathrm{TO}}{}^2 - \omega^2 - i\Gamma_l\omega}\right),$$

$l = ||, \perp$. For the in-plane direction ($l = ||$), the high-frequency permittivity $\varepsilon_{l,\infty} = 5.1$, the longitudinal optical frequency $\omega_{l,\mathrm{LO}} = 1650$ cm^{-1}, the transverse optical frequency $\omega_{l,\mathrm{TO}} = 1394.5$ cm^{-1}, and the phonon damping rate $\Gamma_l = 1.8$ cm^{-1} [44]. For the out-of-plane direction ($l = \perp$), $\varepsilon_{l,\infty} = 2.5$, $\omega_{l,\mathrm{LO}} = 845$ cm^{-1}, $\omega_{l,\mathrm{TO}} = 785$ cm^{-1}, and $\Gamma_l = 1$ cm^{-1} [44]. At 25.35 THz, one has $\varepsilon_{\perp,h\mathrm{BN}} = 0$ and $\varepsilon_{||,h\mathrm{BN}} > 0$.

APPENDIX B: VERIFICATION OF THE EFFECTIVE MEDIUM THEORY

Figure 6 shows the comparison of reflectance calculated from the real structure and from the effective structure at

25.35 THz. As a proof-of-concept demonstration, the real structure is chosen to be a monolayer graphene deposited on top of a h-BN slab with a thickness of 9 nm. For the real structure, the graphene is modeled by a surface conductivity of σ_s and h-BN is modeled by a permittivity of $\bar{\bar{\varepsilon}}_{r,h\mathrm{BN}} = [\varepsilon_{||,h\mathrm{BN}}, \varepsilon_{||,h\mathrm{BN}}, \varepsilon_{\perp,h\mathrm{BN}}]$. For the effective structure, the whole graphene–h-BN heterostructure is modeled by a permittivity of $\bar{\bar{\varepsilon}}_{r,\mathrm{eff}} = [\varepsilon_{||,\mathrm{eff}}, \varepsilon_{||,\mathrm{eff}}, \varepsilon_{\perp,\mathrm{eff}}]$; see Eqs. (7) and (8). Figure 6 shows that the two reflectance curves from the real structure and the effective structure coincide, for both the TE waves and TM waves. From Fig. 6, it is reasonable to argue that the effective medium theory is applicable to our designed structures, which can simplify the design and calculation procedures.

For the effective structure, the reflection coefficient is shown in Eq. (3) for TM waves and in Eq. (5) for TE waves. For the real structure, the reflection coefficient has the same form of Eq. (3) for TM waves and of Eq. (5) for TE waves, but with the following changes: change $\bar{\bar{\varepsilon}}_{2,r} = [\varepsilon_{||,r}, \varepsilon_{||,r}, \varepsilon_{\perp,r}]$ to $\bar{\bar{\varepsilon}}_{r,h\mathrm{BN}} = [\varepsilon_{||,h\mathrm{BN}}, \varepsilon_{||,h\mathrm{BN}}, \varepsilon_{\perp,h\mathrm{BN}}]$; for TM waves, change $r^{\mathrm{TM}}_{1|2}$ to $r^{\mathrm{TM}}_{1|2,\text{ with gra}} = [(k^{\mathrm{TM}}_{z,1}/\varepsilon_{1,r}) + (\sigma_s/\omega\varepsilon_0)(k^{\mathrm{TM}}_{z,1}/\varepsilon_{1,r})(k^{TM}_{z,2}/\varepsilon_{||,h\mathrm{BN}}) - (k^{\mathrm{TM}}_{z,2}/\varepsilon_{||,h\mathrm{BN}})]/[(k^{\mathrm{TM}}_{z,2}/\varepsilon_{||,h\mathrm{BN}}) + (\sigma_s/\omega\varepsilon_0)(k^{\mathrm{TM}}_{z,1}/\varepsilon_{1,r})(k^{\mathrm{TM}}_{z,2}/\varepsilon_{||,h\mathrm{BN}}) + (k^{\mathrm{TM}}_{z,1}/\varepsilon_{1,r})]$, change $r^{\mathrm{TM}}_{2|1}$ to $r^{\mathrm{TM}}_{2|1,\text{ with gra}} = [(k^{\mathrm{TM}}_{z,2}/\varepsilon_{||,h\mathrm{BN}}) + (\sigma_s/\omega\varepsilon_0)(k^{\mathrm{TM}}_{z,1}/\varepsilon_{1,r})(k^{\mathrm{TM}}_{z,2}/\varepsilon_{||,h\mathrm{BN}}) - (k^{\mathrm{TM}}_{z,1}/\varepsilon_{1,r})]/[(k^{\mathrm{TM}}_{z,2}/\varepsilon_{||,h\mathrm{BN}}) + (\sigma_s/\omega\varepsilon_0)(k^{\mathrm{TM}}_{z,1}/\varepsilon_{1,r})(k^{\mathrm{TM}}_{z,2}/\varepsilon_{||,h\mathrm{BN}}) + (k^{\mathrm{TM}}_{z,1}/\varepsilon_{1,r})]$, change $t^{\mathrm{TM}}_{1|2}$ to $t^{\mathrm{TM}}_{1|2,\text{ with gra}} = 2(k^{\mathrm{TM}}_{z,1}/\varepsilon_{1,r})/[(k^{\mathrm{TM}}_{z,2}/\varepsilon_{||,h\mathrm{BN}}) + (\sigma_s/\omega\varepsilon_0)(k^{\mathrm{TM}}_{z,1}/\varepsilon_{1,r})(k^{\mathrm{TM}}_{z,2}/\varepsilon_{||,h\mathrm{BN}}) + (k^{\mathrm{TM}}_{z,1}/\varepsilon_{1,r})]$, and change $t^{\mathrm{TM}}_{2|1}$ to $t^{\mathrm{TM}}_{2|1,\text{ with gra}} = 2(k^{\mathrm{TM}}_{z,2}/\varepsilon_{||,h\mathrm{BN}})/[(k^{\mathrm{TM}}_{z,2}/\varepsilon_{||,h\mathrm{BN}}) + (\sigma_s/\omega\varepsilon_0)(k^{\mathrm{TM}}_{z,1}/\varepsilon_{1,r})(k^{\mathrm{TM}}_{z,2}/\varepsilon_{||,h\mathrm{BN}}) + (k^{\mathrm{TM}}_{z,1}/\varepsilon_{1,r})]$; for TE waves, change $r^{\mathrm{TE}}_{1|2}$ to $r^{\mathrm{TE}}_{1|2,\text{ with gra}} = (k^{\mathrm{TE}}_{z,1} - \sigma_s\omega\mu_0 - k^{\mathrm{TE}}_{z,2})/(k^{\mathrm{TE}}_{z,2} + \sigma_s\omega\mu_0 + k^{\mathrm{TE}}_{z,1})$, change $r^{\mathrm{TE}}_{2|1}$ to $r^{\mathrm{TE}}_{2|1,\text{ with gra}} = (k^{\mathrm{TE}}_{z,2} - \sigma_s\omega\mu_0 - k^{\mathrm{TE}}_{z,1})/(k^{\mathrm{TE}}_{z,2} + \sigma_s\omega\mu_0 + k^{\mathrm{TE}}_{z,1})$, change $t^{\mathrm{TE}}_{1|2}$ to $t^{\mathrm{TE}}_{1|2,\text{ with gra}} = 2k^{\mathrm{TE}}_{z,1}/(k^{\mathrm{TE}}_{z,2} + \sigma_s\omega\mu_0 + k^{\mathrm{TE}}_{z,1})$, and change $t^{\mathrm{TE}}_{2|1}$ to $t^{\mathrm{TE}}_{2|1,\text{ with gra}} = 2k^{\mathrm{TE}}_{z,2}/(k^{\mathrm{TE}}_{z,2} + \sigma_s\omega\mu_0 + k^{\mathrm{TE}}_{z,1})$.

APPENDIX C: REFLECTANCE AND TRANSMITTANCE

Figure 7 shows the reflectance and transmittance, at various incident angles, as a function of the slab thickness at 25.35 THz. The slab is constructed by the graphene–h-BN heterostructure and has a relative permittivity of $\bar{\bar{\varepsilon}}_{r,\mathrm{eff}} = [\varepsilon_{||,\mathrm{eff}}, \varepsilon_{||,\mathrm{eff}}, \varepsilon_{\perp,\mathrm{eff}}]$; see Eqs. (7) and (8). When the loss is neglected, the TM reflectance is close to one, while the TE reflectance is close to zero. Both of them are insensitive to the slab thickness; see Fig. 7(a). When the realistic material loss is considered, the reflectance (transmittance) of TM waves increases (decreases) rapidly with the slab thickness, while the reflectance and transmittance of TE waves are still relatively insensitive to the slab thickness; as shown in Figs. 7(b) and 7(c). This way, for the design of polarizers with the reflected waves, there is a tradeoff for the choice of the slab thickness, since the increase of the slab thickness can increase the TM reflectance in Fig. 7(b) but will degrade the performance of polarization splitting in Fig. 4. For the design of polarizers with the transmitted waves, a thick slab is always preferred, to simultaneously maintain a high-TE transmittance in Fig. 7(c) and a good performance of polarization splitting in Fig. 5.

[1] D. N. Basov, M. M. Fogler, and F. J. García De Abajo, Polaritons in van der Waals materials, Science **354**, aag1992 (2016).

[2] T. Low, A. Chaves, J. D. Caldwell, A. Kumar, N. X. Fang, P. Avouris, T. F. Heinz, F. Guinea, L. Martin-Moreno, and F. Koppens, Polaritons in layered two-dimensional materials, Nat. Mater. **16**, 182 (2017).

[3] F. J. García de Abajo, Special issue "2D materials for nanophotonics", ACS Photon. **4**, 2959 (2017).

[4] A. K. Geim and I. V. Grigorieva, Van der Waals heterostructures, Nature **499**, 419 (2013).

[5] K. S. Novoselov, A. Mishchenko, A. Carvalho, and A. C. Neto, 2D materials and van der Waals heterostructures, Science **353**, aac9439 (2016).

[6] A. Vakil and N. Engheta, Transformation optics using graphene, Science **332**, 1291 (2011).

[7] F. H. L. Koppens, D. E. Chang, and F. J. García De Abajo, Graphene plasmonics: a platform for strong light-matter interactions, Nano Lett. **11**, 3370 (2011).

[8] D. Rodrigo, O. Limaj, D. Janner, D. Etezadi, F. J. García De Abajo, V. Pruneri, and H. Altug, Mid-infrared plasmonic biosensing with graphene, Science **349**, 165 (2015).

[9] L. J. Wong, I. Kaminer, O. Ilic, J. D. Joannopoulos, and M. Soljačić, Towards graphene plasmon-based free-electron infrared to x-ray sources, Nat. Photon. **10**, 46 (2016).

[10] T. G. Folland, O. P. Marshall, Y. Kim, K. S. Novoselov, and S. Chakraborty, Gain modulation by graphene plasmons in aperiodic lattice lasers, Science **351**, 246 (2016).

[11] X. Lin, I. Kaminer, X. Shi, F. Gao, Z. Yang, Z. Gao, H. Buljan, J. D. Joannopoulos, M. Soljačić, H. Chen, and B. Zhang, Splashing transients of 2D plasmons launched by swift electrons, Sci. Adv. **3**, e1601192 (2017).

[12] Z. Li, K. Yao, F. Xia, S. Shen, J. Tian, and Y. Liu, Graphene plasmonic metasurfaces to steer infrared light, Sci. Rep. **5**, 12423 (2015).

[13] W. Ma, Z. Huang, X. Bai, P. Zhan, and Y. Liu, Dual-band light focusing using stacked graphene metasurfaces, ACS Photon. **4**, 1770 (2017).

[14] J. D. Caldwell, A. V. Kretinin, Y. Chen, V. Giannini, M. M. Fogler, Y. Francescato, C. T. Ellis, J. G. Tischler, C. R. Woods, A. J. Giles, M. Hong, K. Watanabe, T. Taniguchi, S. A. Maier, and K. S. Novoselov, Sub-diffractional volume-confined polaritons in the natural hyperbolic material hexagonal boron nitride, Nat. Commun. **5**, 5221 (2014).

[15] S. Dai, Z. Fei, Q. Ma, A. S. Rodin, M. Wagner, A. S. McLeod, M. K. Liu, W. Gannett, W. Regan, K. Watanabe, T. Taniguchi, M. Thiemens, G. Dominguez, A. H. castro Neto, A. Zetti, F. Keilmann, P. Jarillo-Herrero, M. M.

Folger, and D. N. Basov, Tunable phonon polaritons in atomically thin van der Waals crystals of boron nitride, Science **343**, 1125 (2014).

[16] E. Yoxall, M. Schnell, A. Y. Nikitin, O. Txoperena, A. Woessner, M. B. Lundeberg, F. Casanova, L. E. Hueso, F. H. L. Koppens, and R. Hillenbrand, Direct observation of ultraslow hyperbolic polariton propagation with negative phase velocity, Nat. Photon. **9**, 674 (2015).

[17] S. Dai, Q. Ma, T. Andersen, A. S. McLeod, Z. Fei, M. K. Liu, M. Wagner, K. Watanabe, T. Taniguchi, M. Thiemens, F. Keilmann, P. Jarillo-Herrero, M. M. Fogler, and D. N. Basov, Subdiffractional focusing and guiding of polaritonic rays in a natural hyperbolic material, Nat. Commun. **6**, 6963 (2015).

[18] P. Li, M. Lewin, A. V. Kretinin, J. D. Caldwell, K. S. Novoselov, T. Taniguchi, K. Watanabe, F. Gaussmann, and T. Taubner, Hyperbolic phonon-polaritons in boron nitride for near-field optical imaging and focusing, Nat. Commun. **6**, 7507 (2015).

[19] M. Y. Musa, M. Renuka, X. Lin, R. Li, H. Wang, E. Li, and H. Chen, Confined transverse electric phonon polaritons in hexagonal boron nitrides, 2D Mater. **5**, 015018 (2017).

[20] P. Li, I. Dolado, F. J. Alfaro-Mozaz, F. Casanova, L. E. Hueso, S. Liu, J. H. Edgar, A. Y. Nikitin, S. Vélez, and R. Hillenbrand, Infrared hyperbolic metasurface based on nanostructured van der Waals materials, Science **359**, 892 (2018).

[21] C. Qian, X. Lin, Y. Yang, F. Gao, Y. Shen, J. Lopez, I. Kaminer, B. Zhang, E. Li, M. Soljačić, and H. Chen, Multifrequency superscattering from subwavelength hyperbolic structures, ACS Photon. **5**, 1506 (2018).

[22] V. W. Brar, M. S. Jang, M. Sherrott, S. Kim, J. J. Lopez, L. B. Kim, M. Choi, and H. Atwater, Hybrid surface-phonon-plasmon polariton modes in graphene/monolayer h-BN heterostructures, Nano Lett. **14**, 3876 (2014).

[23] S. Dai, Q. Ma, M. K. Liu, T. Anderson, Z. Fei, M. D. Goldflam, M. Wagner, K. Watanabe, T. Taniguchi, M. Thiemens, F. Keilmann, G. C. A. M. Janssen, S. E. Zhu, P. Jarillo-Herrero, M. M. Folger, and D. N. Basov, Graphene on hexagonal boron nitride as a tunable hyperbolic metamaterial, Nat. Nanotechnol. **10**, 682 (2015).

[24] A. Woessner, M. B. Lundeberg, Y. Gao, A. Principi, P. Alonso-González, M. Carrega, K. Watanabe, T. Taniguchi, G. Vignale, M. Polini, J. Hone, R. Hillenbrand, and F. H. L. Koppens, Highly confined low-loss plasmons in graphene-boron nitride heterostructures, Nat. Mater. **14**, 421 (2015).

[25] G. X. Ni, L. Wang, M. D. Goldflam, M. Wagner, Z. Fei, A. S. McLeod, M. K. Liu, F. Keilmann, B. Özyilmaz, A. H. Castro Neto, J. Hone, M. M. Fogler, and D. N. Basov, Ultrafast optical switching of infrared plasmon polaritons in high-mobility graphene, Nat. Photon. **10**, 244 (2016).

[26] X. Lin, Y. Yang, N. Rivera, J. J. López, Y. Shen, I. Kaminer, H. Chen, B. Zhang, J. D. Joannopoulos, and M. Soljačić, All-angle negative refraction of highly squeezed plasmon and phonon polaritons in graphene-boron nitride heterostructures, Proc. Natl. Acad. Sci. U.S.A. **114**, 6717 (2017).

[27] Y. Jiang, X. Lin, T. Low, B. Zhang, and H. Chen, Group-velocity-controlled and gate-tunable directional excitation of polaritons in graphene-boron nitride heterostructures, Laser Photon. Rev. **12**, 180049 (2018).

[28] X. Lin, Z. Wang, F. Gao, B. Zhang, and H. Chen, Atomically thin nonreciprocal optical isolation, Sci. Rep. **4**, 4190 (2014).

[29] P. Y. Chen and A. Alù, Atomically thin surface cloak using graphene monolayers, ACS Nano **5**, 5855 (2011).

[30] S. Thongrattanasiri, F. H. L. Koppens, and F. J. García De Abajo, Complete Optical Absorption in Periodically Patterned Graphene, Phys. Rev. Lett. **108**, 047401 (2012).

[31] P. Lodahl, S. Mahmoodian, S. Stobbe, A. Rauschenbeutel, P. Schneeweiss, J. Volz, H. Pichler, and P. Zoller, Chiral quantum optics, Nature **541**, 473 (2017).

[32] D. H. Goldstein, *Polarized Light* (CRC Press, Boca Raton, FL, 2010).

[33] B. Shen, P. Wang, R. Polson, and R. Menon, An integrated-nanophotonics polarization beamsplitter with 2.4×2.4 μm^2 footprint, Nat. Photon. **9**, 378 (2015).

[34] Y. Zhang, Y. He, X. Jiang, B. Liu, C. Qiu, Y. Su, and R. A. Soref, Ultra-compact and highly efficient silicon polarization splitter and rotator, APL Photon. **1**, 91304 (2016).

[35] L. Li and J. A. Dobrowolski, High-performance thin-film polarizing beam splitter operating at angles greater than the critical angle, Appl. Opt. **39**, 2754 (2000).

[36] X. Lin, Y. Shen, I. Kaminer, H. Chen, and M. Soljačić, Transverse-electric Brewster effect enabled by nonmagnetic two-dimensional materials, Phys. Rev. A **94**, 23836 (2016).

[37] V. Mocella, P. Dardano, L. Moretti, and I. Rendina, A polarizing beam splitter using negative refraction of photonic crystals, Opt. Express **13**, 7699 (2005).

[38] X. Ao, L. Liu, L. Wosinski, and S. He, Polarization beam splitter based on a two-dimensional photonic crystal of pillar type, Appl. Phys. Lett. **89**, 171115 (2006).

[39] J. Zhao, Y. Chen, and Y. Feng, Polarization beam splitting through an anisotropic metamaterial slab realized by a layered metal-dielectric structure, Appl. Phys. Lett. **92**, 071114 (2008).

[40] H. F. Ma, G. Z. Wang, W. X. Jiang, and T. J. Cui, Independent control of differently-polarized waves using anisotropic gradient-index metamaterials, Sci. Rep. **4**, 6337 (2014).

[41] T. Cai, G. M. Wang, X. F. Zhang, J. G. Liang, Y. Q. Zhuang, D. Liu, and H. X. Xu, Ultra-thin polarization beam splitter using 2-D transmissive phase gradient metasurface, IEEE Trans. Antennas Propag. **63**, 5629 (2015).

[42] D. G. Baranov, J. H. Edgar, T. Hoffman, N. Bassim, and J. D. Caldwell, Perfect interferenceless absorption at infrared frequencies by a van der Waals crystal, Phys. Rev. B **92**, 201405 (2015).

[43] J. Wu, L. Jiang, J. Guo, X. Dai, Y. Xiang, and S. Wen, Tunable perfect absorption at infrared frequencies by a graphene-hBN hyper crystal, Opt. Express **24**, 17103 (2016).

[44] J. A. Kong, *Electromagnetic Wave Theory* (EMW Publishing, Cambridge, MA, 2008).

[45] T. Q. P. Vuong, S. Liu, A. Van der Lee, R. Cuscó, L. Artús, T. Michel, P. Valvin, J. H. Edgar, G. Cassaboisand, and B. Gil, Isotope engineering of van der Waals interactions in hexagonal boron nitride, Nat. Mater. **17**, 152 (2018).

[46] A. J. Giles, S. Dai, I. Vurgaftman, T. Hoffman, S. Liu, L. Lindsay, and J. G. Tischler, Ultralow-loss polaritons in isotopically pure boron nitride, Nat. Mater. **17**, 134 (2018).
[47] X. Lin, N. Rivera, J. J. López, I. Kaminer, H. Chen, and M. Soljačić, Tailoring the energy distribution and loss of 2D plasmons, New J. Phys. **18**, 105007 (2016).
[48] K. I. Bolotin, K. J. Sikes, Z. Jiang, M. Klima, G. Fudenberg, J. Hone, P. Kim, and H. L. Stormer, Ultrahigh electron mobility in suspended graphene, Solid State Commun. **146**, 351 (2008).
[49] C. R. Dean, A. F. Young, I. Meric, C. Lee, L. Wang, S. Sorgenfrei, K. Watanabe, T. Taniguchi, P. Kim, K. L. Shepard, and J. Hone, Boron nitride substrates for high-quality graphene electronics, Nat. Nanotechnol. **5**, 722 (2010).
[50] C. Ye, Z. Zhu, W. Xu, X. Yuan, and S. Qin, Electrically tunable absorber based on nonstructured graphene, J. Opt. **17**, 125009 (2015).
[51] K. S. Novoselov, K. G. Andre, V. M. Sergei, D. Jiang, Y. Zhang, V. D. Sergey, V. G. Irina, and A. F. Alexandr, Electric field effect in atomically thin carbon films, Science **306**, 666 (2004).
[52] N. Engheta, Pursuing near-zero response, Science **340**, 286 (2013).
[53] I. Liberal and N. Engheta, Near-zero refractive index photonics, Nat. Photon. **11**, 149 (2017).